3D Active Edge Silicon Detector Tests With 120 GeV Muons

Cinzia Da Via, Mario Deile, Jasmine Hasi, Christopher Kenney, Angela Kok, Sherwood Parker, Stephen Watts, Giovanni Anelli, Valentina Avati, Valerio Bassetti, Vittorio Boccone, Marco Bozzo, Karsten Eggert, Fabrizio Ferro, Alexandre Inyakin, Jan Kaplon, Julio Lozano Bahilo, Aldo Morelli, Hubert Niewiadomski, Elias Noschis, Fredrik Oljemark, Marco Oriunno, Kenneth Österberg, Gennaro Ruggiero, Walter Snoeys, and Stefan Tapprogge

***Abstract*—3D detectors with electrodes penetrating through the silicon wafer and covering the edges were tested in the SPS beam line X5 at CERN in autumn 2003. Detector parameters including efficiency, signal-to-noise ratio, and edge sensitivity were measured using a silicon telescope as a reference system. The measured sensitive width and the known silicon width were equal within less than 10 μm.**

***Index Terms*—3D silicon detectors, active edges, forward proton tagging, large hadron collider, radiation hardness, Roman pots.**

I. Introduction

THE measurement of elastic and most diffractive pp-scattering processes requires the detection of protons produced at very small scattering angles, which is traditionally accomplished by inserting detectors into the beam pipe using so-called Roman Pots (RPs) where the detectors are separated from the primary beam vacuum by only a 150 μm thick steel window.

The TOTEM experiment [1] will perform such measurements at the LHC. Its RPs will be installed at 147 m and 220 m from IP5. TOTEM's main physics objective is the measurement of the total pp cross-section with an absolute error of about 1 mb by using the luminosity independent method based on the Optical Theorem, which requires the simultaneous measurement of the inelastic pp interaction rate and the elastic pp scattering cross-section down to the squared four-momentum transfer of $-\mathrm{t}\sim 10^{-3}$ GeV^2 corresponding to scattering angles of only a few μrad [1].

In order to detect protons so close to the beam, the detector edge has to approach the beam axis to a distance of about 1 mm. With a typical LHC beam width of $\sigma_{\mathrm{beam}} \approx 80$ μm at 220 m for the TOTEM optics with $\beta^* = 1540$ m, the outer surface of the RP window can safely approach the beam to about 10 $\sigma_{\mathrm{beam}} \approx 0.8$ mm. The thin window on this surface adds another 0.15 mm to the minimum possible distance of the detectors from the beam.

To avoid additional inefficient space, the detectors should be active to within 50–60 μm or less from their physical edges, which if sawed, may also be chipped and have small cracks. In general, planar silicon detectors have a wide (0.25–1 mm) insensitive border region around the sensitive area that is occupied by a sequence of guard rings. This ring structure controls the potential distribution between the detector's sensitive area and the cut edge in order to produce a uniform electric field reduction at the detector periphery. A last, non-floating, inner guard ring may also be used to intercept the surface leakage current. Detectors designed for a heavy radiation environment or generally for operation at high bias voltages, contain multi-ring structures with typically about 20 rings.

The close approach of the detectors to the beam also represents a challenge for the radiation hardness of the detector and front-end electronics. The detector system has to be robust, and for satisfactory control of systematic uncertainties its position has to be aligned and maintained within 50 μm.

3D detectors, as proposed by S. Parker in 1995 [2], with "active edges" as proposed by C. Kenney [3], [4] in 1997, can fulfill all the above-mentioned requirements and are possible candidates for a later upgrade of TOTEM's Roman Pot detectors.

This technology combines micro-machining and standard VLSI (Very Large Scale Integration) processing and takes full advantage of high precision deep-etching techniques in silicon. Since the original publication several prototypes with different dimensions and electrode configurations have been fabricated and fully characterized. Besides the TOTEM experiment, other applications such as the LHC inner pixel layer replacement and upgrades for the SuperLHC, the Compact Linear Collider (CLIC) and medical applications might benefit from the features of the 3D technology [5]–[9].

Manuscript received November 29, 2007; revised November 17, 2008. Current version published April 08, 2009. This work was supported in part by the U.S. Department of Energy under Grants DE-FG02-04ER41291 and DE-FG02-05ER41387 (ADR), and was performed in part at the Stanford Nanofabrication Facility (a member of the National Nanotechnology Infrastructure Network), which is supported by the National Science Foundation under Grant ECS-9731293.

C. Da Via, J. Hasi, and S. Watts are with the Physics and Astronomy Department, University of Manchester, MI3 9PL Manchester, U.K. (e-mail: cinzia.da.via@cern.ch).

M. Deile, G. Anelli, K. Eggert, A. Inyakin, J. Kaplon, J. Lozano Bahilo, H. Niewiadomski, E. Noschis, M. Oriunno, G. Ruggiero, and W. Snoeys are with the PH Department, CERN, 1211 Genève 23, Switzerland (e-mail: Mario.Deile@cern.ch).

C. Kenney is with the Molecular Biology Consortium, Stanford Nanofabrication Facility, Palo Alto, CA 94303 USA.

A. Kok is with SINTEF, MinaLab, Olso, Norway.

S. Parker is with the University of Hawaii, c/o Lawrence Berkeley Lab, Berkeley CA 94720 USA (e-mail: sher@slac.stanford.edu).

V. Avati, F. Oljemark, K. Österberg, and S. Tapprogge are with the Department of Physical Sciences, High Energy Physics Division, University of Helsinki and Helsinki Institute of Physics, Helsinki, Finland.

V. Bassetti, V. Boccone, M. Bozzo, F. Ferro, and A. Morelli are with INFN Sez. di Genova and Universitá di Genova, Genova, Italy.

Color versions of one or more of the figures in this paper are available online at http://ieeexplore.ieee.org.

Digital Object Identifier 10.1109/TNS.2009.2013951

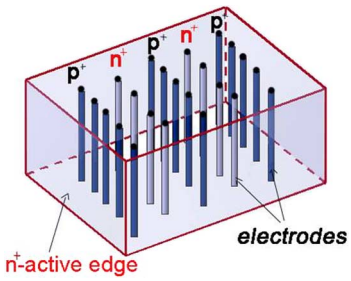

Fig. 1. Sketch of a pure 3D detector where the p+ and n+ electrodes are inside the silicon bulk. The edges are electrodes (active edges) that surround the sides of the 3D device making an active volume sensitive to a few μm from the physical edge.

II. 3D Silicon Detector Main Features

Fig. 1 sketches the main features of the novel 3D detector design. In 3D technology, contrary to the standard planar silicon configuration, the electrodes are fabricated inside the bulk of the silicon wafer instead of being implanted on its surface. The consequences of this approach are manifold:

1. Maximum collection distances can be as short as 50 μm or less for all of the charge generated by the traversing particle in a thick substrate (normally about 24 000 e^- for a 300 μm thick silicon substrate).
2. The response can be an order of magnitude faster than in planar structures due to the shorter drift distances and near-simultaneous arrival times for all charges from tracks parallel to the electrodes.
3. 3D electrodes have a larger surface area than the corresponding planar electrodes, resulting in a higher average field for a given peak field.
4. Radiation hardness [5], [10], [11] is increased due to the short carrier drift distances and higher electric fields which reduce carrier trapping.
5. Both electrode types are accessible from the front and back side of the wafer and can be joined by conductors in a number of different ways for pixel and micro-strip readouts with either polarity.
6. The sensor edges can also be made into electrodes.

These "active edges" are made by etching a trench around the detector's physical edge and then diffusing in dopant to make an electrode. The electric field lines, which are parallel to the wafer's surface, can then be properly terminated at this "edge" electrode. Additional details including the growth of an oxide cap, filling of the trench for later lithography steps and the dicing etch have been presented in [7].

A similar processing technique was used to fabricate "planar/3D" devices with planar central electrodes and 3D-active edges [7]. In this configuration, the free edges of a planar detector are again deep etched and n+ dopant diffused in.

All these processes require the use of a support wafer that provides mechanical strength and supports the devices during and after the active edge etch. The removal of this support takes place after a dicing etch which penetrates the device wafer and completely surrounds each device perimeter. Fig. 2 shows a schematic diagram of part of two active edge sensors prior to that removal.

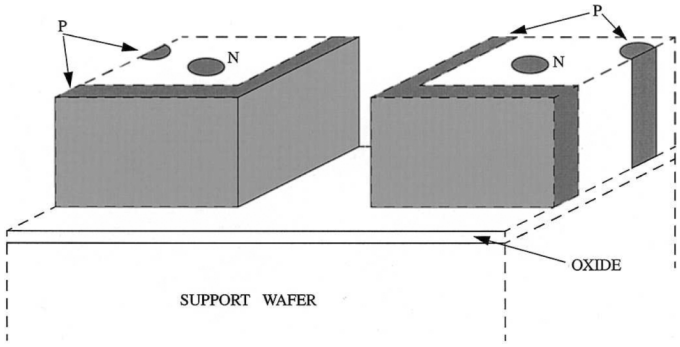

Fig. 2. Schematic view (not to scale) of part of two adjacent active edge detectors after (1) the electrode hole and trench etching (2) the doped polycrystalline electrode deposition, (3) the dicing etch, but still bonded, with an oxide layer, to their support wafer. The visible parts of the doped polycrystalline silicon electrodes are shaded. For simplicity, metal conductors are not shown. The cut face (dashed lines) shows a view of the interior.

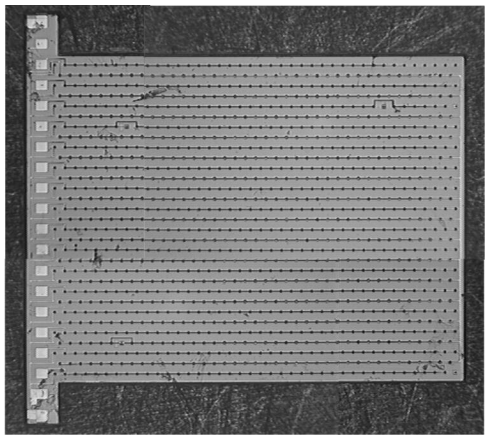

Fig. 3. Photograph of a 3D detector with a microstrip readout configuration. The circular electrode tops are clearly visible. Aluminum strips tie the p+ and n+ electrodes together. The p+ (signal) strips end at the bonding pads (left edge of figure). The n+ (bias) strips end at the border metal strip (right edge) which continues along the top and bottom and goes to the end pads.

Some advantages of active edges are:

1. The edge leakage current, usually present after the device has been saw-cut, is suppressed.
2. The dead area which would be otherwise needed for guard rings, chips and cracks resulting from sawing, and to control the bulge of the electric field in planar detectors is reduced to no more than a few microns.
3. There is no need for outer rings of 3D guard electrodes (an approximate 3D analog of planar guard rings such as those shown in Fig. 13 of [3]).

The irradiation and characterization of several samples have been performed at room temperature. A full depletion bias voltage of 105 V has been measured for a device irradiated with 10^{15} 55 MeV protons/cm^2, corresponding to 1.8×10^{15} n/cm^2 (following the Non Ionizing Energy Loss scaling [12]–[14]), while the charge collection efficiency has been measured to be more than 90% after 1×10^{15} protons/cm^2. Simulations predict that 3D detectors should work beyond 5×10^{15} n/cm^2, in particular if oxygen enriched substrates and electron signal readout are employed [11], [14], [15].

Fig. 3 shows a detector with micro-strip connections, with electrodes of the same type connected by aluminum strips. The

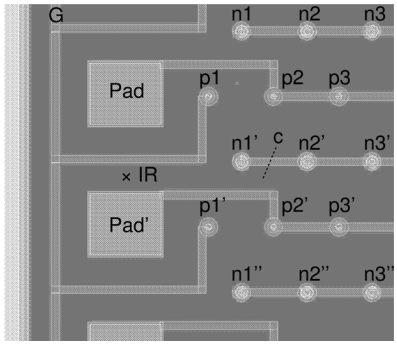

Fig. 4. Layout diagram showing from the top, (1) a p+ guard connector (G) and n+ bias line and electrodes (n1–n3); (2) a signal electrode pad (Pad), p+ guard electrode (p1) and signal electrodes (p2, p3) and connectors; (3) a repeat of the above. A portion of the active edge, which completely surrounds the sensor, can be seen at the far left. The dashed cut line c and the infrared illumination region centered on the point IR are only relevant for the tests discussed in Section 10.1.

readout pads are visible along the left edge of the picture. The pad region was not designed for track detection, but has some sensitivity which is discussed in Chapter VI. The active edge continues along all 4 sides of the sensor. Fig. 4 shows a layout diagram of a section of the sensor, showing several pads, electrodes, and connecting signal and bias strips in more detail.

These devices were used for the tests presented in this paper. All had 'active edges'.

Note that proposed uses of active edge sensors in the far-forward regions at the LHC anticipate the use of pixel sensors bump-bonded to VLSI pixel readout chips. Unlike sensors, the active region of readout chips is very thin and modern diamond saws, which can have positioning accuracies of 1 micron or less, can routinely make cuts within 10–15 microns of the active part of a circuit, with no cracks or chips penetrating into the circuit.

III. SPS Test Beam Measurement Setup

The aim of the 120 GeV muon test beam experiment in the CERN-SPS beam line X5 was to test the operation and edge response of 3D detectors in a high-energy particle beam. The 3D detector resolution and system efficiency were measured with reference to a beam telescope [16] consisting of six silicon microstrip detectors with a strip pitch of 50 μm and an area of 5×5 cm^2. A typical hit cluster occupied between 1 and 3 strips. This configuration results in an average resolution of about 8 μm per plane if the charge sharing for multi-strip clusters is taken advantage of. Four of the planes of the telescope had their strips in the same orientation (horizontal) as the 3D detectors' strips. Hence the vertical track intercept (y) at the 3D detector was predicted with a precision of about 4 μm. The second (horizontal) coordinate of the tracks was measured by the remaining two telescope planes whose strips were orientated vertically. The horizontal (x) precision at the 3D detector was around 15 μm.

Four 3D detectors, such as the one shown in Fig. 3, were placed at the center of the silicon telescope. A diagram of the apparatus in the SPS muon beam-line is shown in Fig. 5. Detector number 1 had a broken edge strip, but was otherwise functional; detector number 2, when installed on the beam line, became noisy, and detector 4 had a bad connection to the readout. Thus, the following results come from detectors 1 and 3.

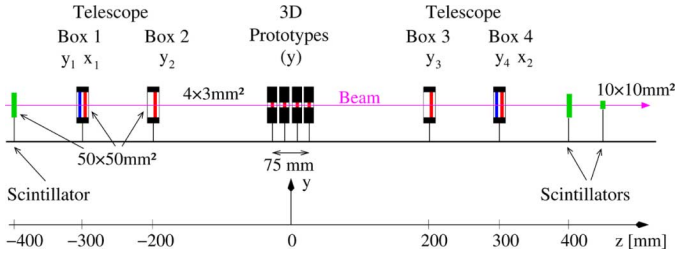

Fig. 5. Schematic drawing of the X5 test beam layout in August/September 2003. The boxes 1–4 constitute the silicon reference telescope "ODYSSEUS" [16] with four detectors measuring the y projection and two detectors measuring x. The 3D detectors were in the same orientation as the telescope planes in the y projection.

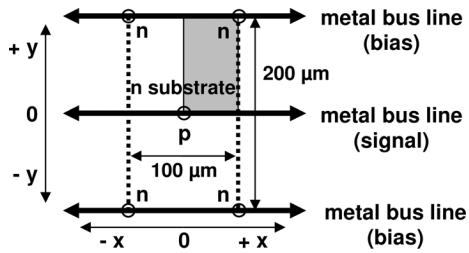

Fig. 6. Definition of a single non-edge cell in the detector consisting of a p-electrode in the center and one quarter of the n-electrodes in each corner. The statistics were further improved with the mapping onto one cell quadrant (grey rectangle). The p-p and n-n connecting aluminum strips are horizontal in this figure.

The 3D sensors under study were fabricated at the Stanford Nanofabrication Facility (SNF), USA [17] using n-type high resistivity silicon substrates with four n-type active edges surrounding the device. They were fully depleted at 25 V, and were operated at 40 V. They had 16 rows parallel to the x-axis each having 38 p+ signal electrodes spaced by 100 μm. Rows of n+ electrodes were between the p+ rows, separated in y from them by 100 μm. Each n+ electrode was midway in x between the p+ electrodes. A typical cell layout is shown in Fig. 6.

Neglecting the end under the bonding pads, each sensor had a total width in y of 3.195 mm, a length of 3.948 mm, and a thickness of 180 μm.

Each row of p-electrodes of the detector was wire-bonded to one input channel of an ATLAS SCTA128VG analogue readout chip [18], [19], originally developed for the SCT silicon tracker for the ATLAS experiment. The hybrid board with both the detector and the front-end chip mounted is shown in Fig. 7. The larger chip on the left is the readout chip wire-bonded to the 3D detector shown on the right.

The analogue SCTA circuit has 128 channels (only 16 were wire-bonded to the detector). Each channel consists of a front-end amplifier and a 128 cell analogue pipeline. The amplifier has an rms noise of 720 electrons and a peaking time of 20 ns. The instantaneous pulse height from each amplifier is stored in successive cells of the analogue pipeline every 25 ns (the beam-crossing interval of the LHC). Particles traverse the detector randomly with respect to the 40 MHz clock provided by a sequencer (SEQSI). The trigger signal, defined by a coincidence of two 5 cm $\times$ 5 cm and one 1 cm $\times$ 1 cm scintillator, is used to start a time-to-digital converter (TDC). A signal synchronized with the clock stops the TDC and selects a cell of

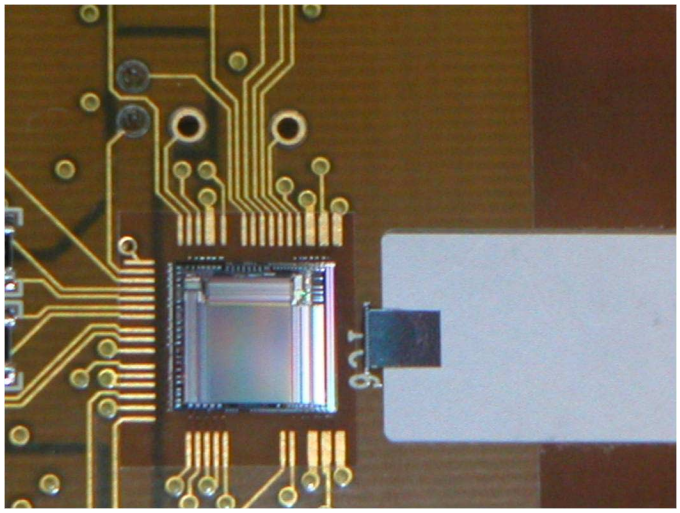

Fig. 7. The hybrid board carrying the 3D detector (right) wire-bonded to the SCTA readout chip (left). Here the readout chip is far larger than the sensor. However, in their proposed uses as far-forward or as inner-layer pixel detectors, 3D active edge sensors would be bump-bonded to readout chips with a matching boundary on the 3 sides that do not have wire-bond pads and which can be routinely cut with precision diamond saws to within 10–15 μm of the active circuitry.

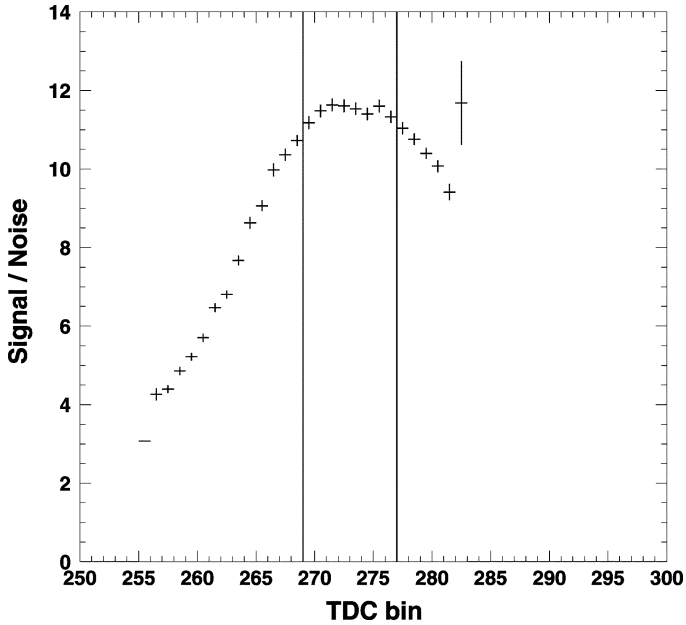

Fig. 8. Signal-to-noise (3 σ -truncated means) of a 3D prototype detector as a function of the trigger time with respect to the internal clock of the 3D readout electronics (with a constant offset). The cuts excluding out-of-time events are displayed as vertical lines. One TDC bin equals 1 ns.

the analogue pipeline for all channels. The cell contents from all channels are then read out and multiplexed into a SIROCO Flash-ADC.

The TDC time window within which a trigger pulse has to arrive in order to coincide with the peak of the corresponding 3D detector pulse needed careful adjustment, which made the system susceptible to timing problems. Fig. 8 shows the typical dependence of the signal-to-noise ratio (and hence of the sampled pulse height) on the TDC timing. Only events occurring between the two TDC cuts drawn were in time and could be accepted for the analysis.

IV. Signal-to-Noise Ratio

In order to avoid radio frequency pick-up and light-induced noise, a light-tight metal box was constructed to cover the 3D planes and to ensure a proper ground definition. Since no cooling was available during the test, the temperature rose considerably above 20°C in the course of long data taking. While a laboratory test with β^- articles from a ^{90}Sr source had yielded a most probable signal-to-noise ratio of 14:1, the signal-to-noise-ratio distribution shown in Fig. 9 obtained from the muon test beam has a most probable value of about 11:1. This can be explained partly by an increase in leakage current, and therefore noise, from increasing temperature, partly by the 30 m long data transmission cables that were not optimized for fast signals, and partly by the retention of electrons on the adjacent bias electrodes, covered in Chapter VIII. The theoretical number of electrons generated by a minimum ionizing particle in 180 μm thick silicon is expected to be 14400. The nominal noise of the system including the detector's capacitance and bonding wires was estimated to be 990 electrons. This corresponds to a signal-to-noise ratio of 14.6:1. For a detector thickness of 300 μm and similar noise figures the expected S/N would be 23:1.

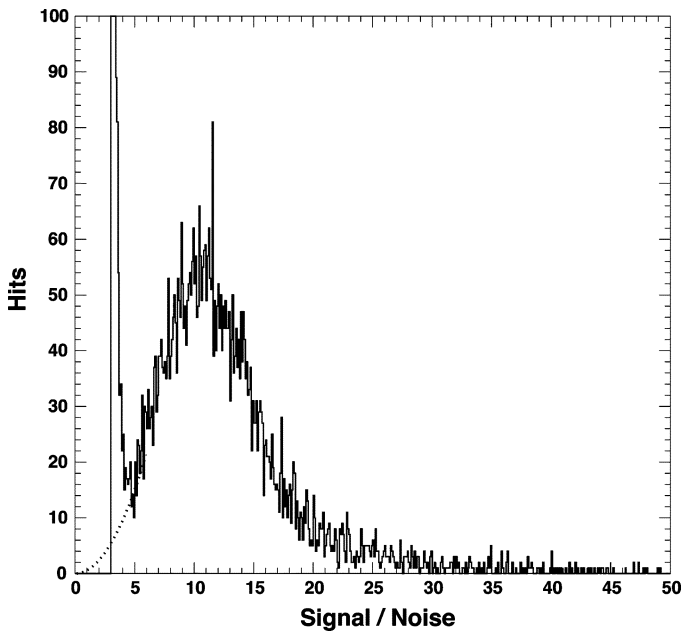

Fig. 9. Signal-to-noise (S/N) distribution obtained for a 3D detector using the events within the time window shown in Fig. 8. A cut $\mathrm{S/N} > 3$ was applied. The spike around $\mathrm{S/N} = 3$ is the tail of the noise distribution.

V. Tracking

The silicon telescope gave the path of each particle track. It therefore predicted the position of a particle passing through each of the 3D detector planes under test. Since the dimension of the reference silicon planes was larger than the 3D planes, it was possible to precisely measure the sensitive area of each 3D detector together with its efficiency. Data for detector 3 will be shown in Figs. 9–14. Data for detector 1 are similar.

The hit search in the 3D detector proceeded as follows:

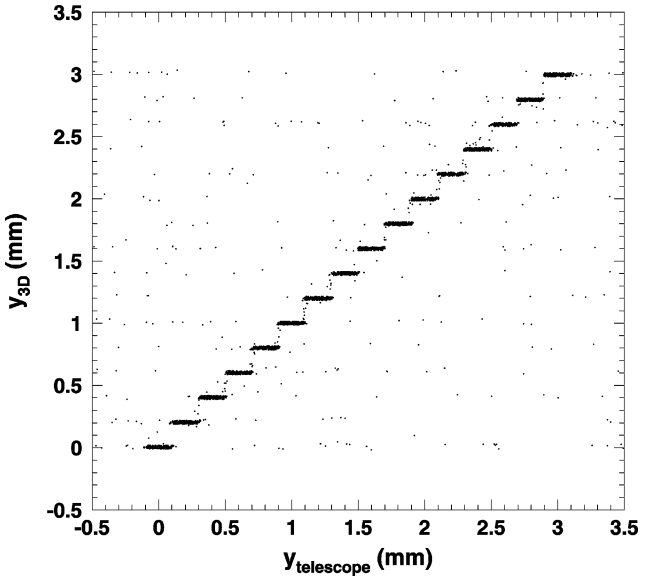

Fig. 10. Correlation between the hit positions y(3D) measured by the 3D detector and the predicted track position $\mathrm{y_{telescope}}$ of the silicon telescope.

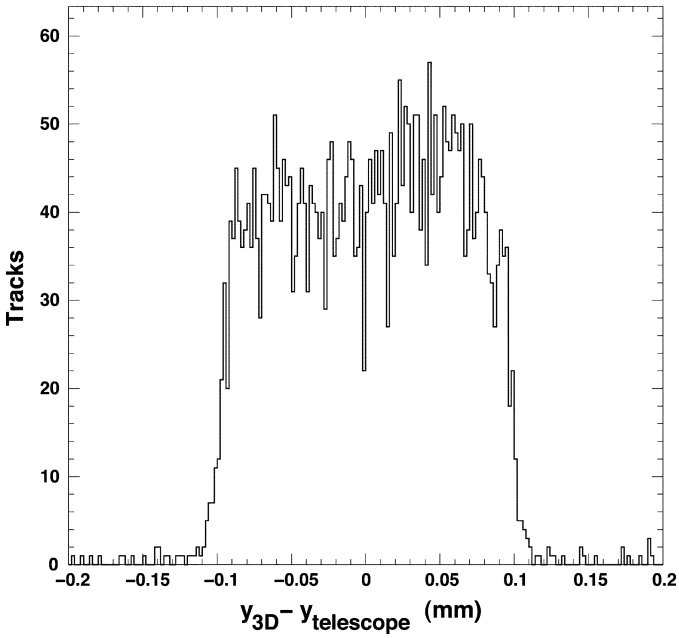

Fig. 11. Residuals $\mathrm{y_{3D}} - \mathrm{y_{telescope}}$. The box distribution resolves well the strip pitch of the 3D detector of 200 μm. The measured rms of 58 μm is close to the expected 200 $\mu\mathrm{m}/\sqrt{12} = 57$ μm.

1. For the selected events, calculate mean, common mode fluctuations (which were small) and rms noise values for the ADC distributions.
2. Repeat step 1 for ADC values within ± 3 sigma of the mean (which is dominated by noise) to get a pedestal mean and rms.
3. For each event, subtract from the ADC value this pedestal mean and common mode value and divide by the pedestal rms.
4. Each strip signal with a S/N greater than or equal to 5 was considered a hit located at the strip center. Due to negative feed-through to neighboring strips (see Chapter VIII), conventional algorithms exploiting charge sharing for resolution improvement could not be applied. The resulting S/N distribution, averaged over the entire detector, for $\mathrm{S/N} > 3$ (to show some of the noise), is given in Fig. 9.

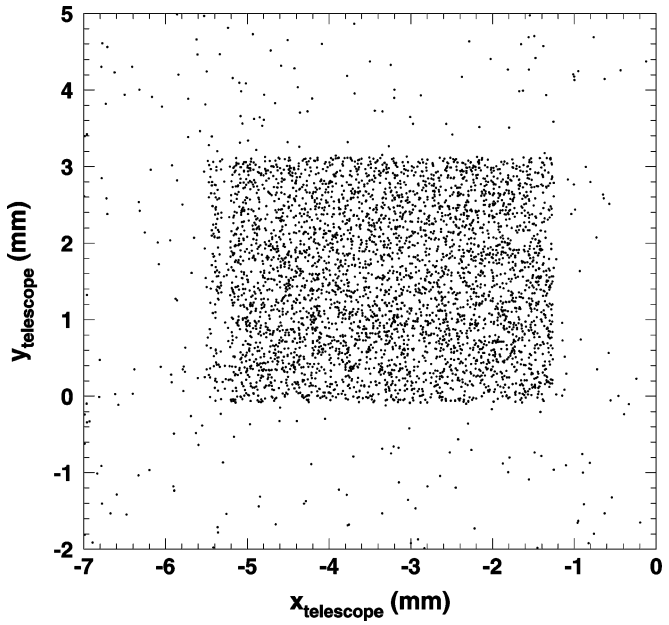

Fig. 12. Two-dimensional hit map of the fully operational 3D detector 3. A point is plotted at the position (x, y) predicted by the telescope as a valid track if also a hit was recorded by the 3D detector. For the inefficient band near the left edge see the text. The upper and lower y edges were used for active edge measurements.

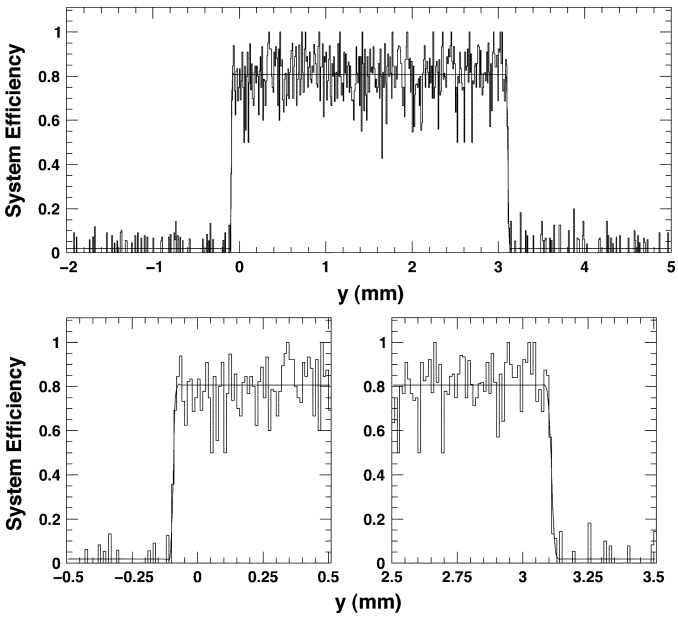

Fig. 13. Projection onto the y axis, of the central part of the data of Fig. 12 for -5 mm $< x < -1.5$ mm (away from the bonding pads and edges), giving the sensor efficiency as a function of y. It was fitted with (1) to give a measure of the sensitive area of the detector.

The telescope tracks along the more accurate y-direction showed good correlation with the hit positions reconstructed from the 3D detector under test. The correlation plot is shown

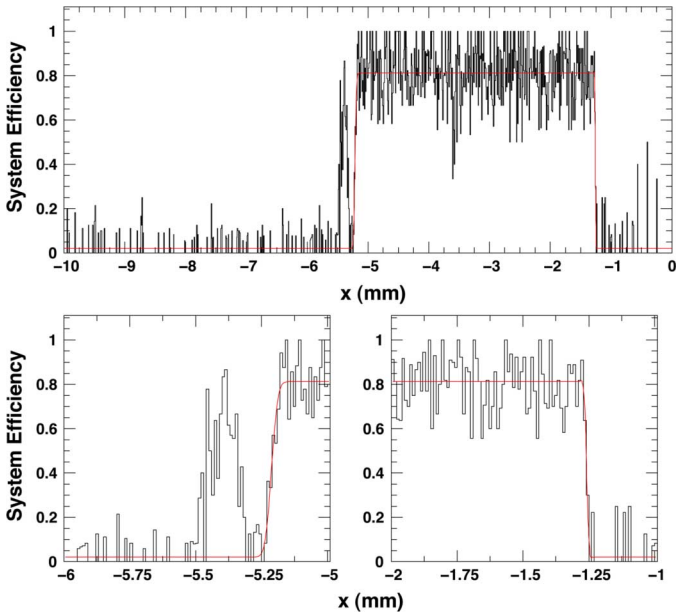

Fig. 14. Projection of the data of Fig. 12 onto the x axis, giving the sensor efficiency as a function of x.

in Fig. 10. The larger bands visible in the plot are due to the different strip pitch between 3D (200 μm) and the reference telescope (50 μm).

This is further seen in the track residual distribution data from the silicon telescope and the detector, $y_{3D} - y_{\text{telescope}}$, plotted in Fig. 11, that shows a box-like structure with a width well in agreement with the 3D detectors' strip pitch of 200 μm. The small quadratic difference between the distribution's rms and the expected value of 200 μm/$\sqrt{12}$ comes from the small but non-zero resolution of the telescope.

VI. Efficiency Measurements

Using the telescope predictions for both track projections, the two-dimensional hit maps of the 3D detectors were recorded. For each track predicted to traverse a 3D detector, the intersection strip was determined. If this strip or one of its direct neighbors had recorded a hit, the 3D detector was said to be efficient in the predicted intersection point. Hits, plotted in Fig. 12, also represent the local efficiency as the track density is nearly uniform. The hit scatter plot shown in Fig. 12 renders well the detector shape. The low hit intensity region beyond the fiducial region at around $x = -5.25$ mm (also visible in Fig. 14) was caused by p-type guard electrodes (p1, p1' electrodes in Fig. 4) that were not connected to the output. The volume under the bonding pads around $x = -5.4$ mm again was sensitive due to a conducting electron sheet attracted by the combination of the pad charge and the normal fixed positive oxide charge at the silicon-oxide interface. The sheet conducted leakage and signal charges from the silicon substrate away to the electrode p2 (see Fig. 4), providing, in effect, a substrate electrode that kept the volume below depleted with a collecting electric field.

TABLE I
Results of the Efficiency Fit Shown in Fig. 13

Parameter	Fit Result
Width y_u - y_l	(3.203 ± 0.004) mm (Expectation: 3.195 mm)
Lower edge : σ_l	(4.3 ± 4.1) µm
10 % – 90 % interval	(11.0 ± 4.2) µm
Upper edge: σ_u	(9.7 ± 3.0) µm
10 % – 90 % interval	(25.0 ± 8.0) µm
Plateau η_0	(80.8 ± 0.6) %
Background b	(1.8 ± 0.1) %
χ^2 / degs. of freedom	1183 / 994

A. Active Edge Measurement

The two-dimensional hit map in Fig. 12 provided a good source for measuring the dimensions of the active region for a 3D detector. This was compared with the dimension given by photolithography to identify the width of the dead region of a 3D active edge detector. Fig. 13 shows the region -5 mm $< x < -1.5$ mm (i.e., away from the bonding pads) projected onto the y axis, after normalization with the predicted track intersection map, which produces a one-dimensional efficiency curve for easier quantification and visualization. Analogously, Fig. 14 shows a projection onto the x axis.

Fig. 13 was fitted with the function

$$\eta(y) = \frac{1}{4}\eta_0 \left[1 + \operatorname{erf}\left(\frac{y - y_l}{\sigma_l\sqrt{2}}\right)\right] \times \left[1 + \operatorname{erf}\left(\frac{y_u - y}{\sigma_u\sqrt{2}}\right)\right] + b. \quad (1)$$

Equation (1) describes a box distribution with Gaussian smearing (with widths σ_l and σ_u at the lower and upper edge respectively) and a background b. The fitted parameters are given in Table I. The plateau gives the detector's efficiency and the fitted width the detector's active area in the y-direction. The results in Table I show that the detector's width known from the photolithography process is reproduced by the efficiency curve within two statistical standard deviations, confirming the minimal dead-edge of 3D detector technology. This property is further underlined by the steep efficiency rise from 10 % to 90 % in an average distance of 18 ± 7 μm.

B. Plateau Efficiency

From the fit shown in Section VI.A, the efficiency was measured for both detectors under test. The measured plateau efficiency of 81 % of the fully operational detector in plane 3 however is surprisingly low. The second 3D detector system used in this study (plane 1) had a very similar efficiency of 79 %. Given the signal-to-noise distribution shown in Fig. 9, one would expect a much higher efficiency. That efficiency can be estimated by integration of the measured Landau distribution including counts that were covered by noise. This was done by extrapolating the start of the measured Landau distribution from $5\sigma_{\text{noise}}$ back to 0. This gives the expected total number of true counts in the 3D detectors. The counts registered by the detectors are

TABLE II
MEASURED AND CALCULATED HIT AND MISS PROBABILITIES

Measured # events	**Measured probabilities**	**Values for joint probabilities assuming independence:**
a ≡ N($\bar{1}$ & $\bar{3}$) = 124	P($\bar{1}$ & $\bar{3}$) = a / t = 0.165 ± 0.014	$P_{indep}(\bar{1}\ \&\ \bar{3}) = [1 - P_m(1)] \times [1 - P_m(3)] = 0.040 \pm 0.004$
b ≡ N($\bar{1}$ & 3) = 36	P($\bar{1}$ & 3) = b / t = 0.048 ± 0.008	$P_{indep}(\bar{1}\ \&\ 3) = [1 - P_m(1)] \times P_m(3) = 0.173 \pm 0.012$
c ≡ N(1 & $\bar{3}$) = 18	P(1 & $\bar{3}$) = c / t = 0.024 ± 0.006	$P_{indep}(1\ \&\ \bar{3}) = P_m(1) \times [1 - P_m(3)] = 0.149 \pm 0.012$
d ≡ N(1 & 3) = 574	P(1 & 3) = d / t = 0.763 ± 0.016	$P_{indep}(1\ \&\ 3) = P_m(1) \times P_m(3) = 0.639 \pm 0.017$
c + d = N(1) = 592	$P_m(1) = (c + d) / t = 0.787 \pm 0.015$	
b + d = N(3) = 610	$P_m(3) = (b + d) / t = 0.811 \pm 0.014$	
t = a + b + c + d = 752		

all the hits that have a signal-to-noise ratio above 5. The ratio between the two gives the expected efficiency

$$\eta(\text{from } S/N) \approx \frac{\int_5^{50} \Lambda_{\text{meas}}(x)\,dx}{\int_5^{50} \Lambda_{\text{meas}}(x)\,dx + \int_0^{5} \Lambda_{\text{extrapol}}(x)\,dx}. \quad (2)$$

The result, 96%, is 16% higher than the measured efficiency. Recombination, and hence inefficiency, in the polycrystalline silicon of the electrode volume cannot explain the 80 %. The 3D detectors employed for this test consist of rectangular cells, each 100 μm × 200 μm. Each cell has two electrodes with a radius of 9 μm. Hence a fraction of 2.5 % of the entire cell area is occupied by electrodes. Assuming, for a lower limit, that the electrodes are totally insensitive (which is not the case as can be seen in the following section) and the particles are passing through the detector perpendicularly to its surface, a detector efficiency of about 98 % is expected.

One possible reason for the discrepancy in the measurement could be the timing difference between the data taken by the telescope and the 3D detectors. The efficiencies of the 3D detectors were measured relative to the entire system, so any systematic counting error in the readout electronics would be included. The problematic timing with respect to the rest of the setup (in particular the telescope) was already mentioned in Chapter III. The true reasons are difficult to identify, but investigating the correlations between the two 3D detectors allows us to identify systematic effects in the data chain if any. If there is no systematic effect, the two detectors should be independent, i.e., there should be no correlation between them. This implies that their combined hit or miss probabilities should factorize:

a. No hits :
$$P_{\text{independent}}(\bar{1}\,\&\bar{3}) = P(\bar{1}) \times P(\bar{3}) \quad (3a)$$
b. Hit in D3 only :
$$P_{\text{independent}}(\bar{1}\,\&3) = P(\bar{1}) \times P(3) \quad (3b)$$
c. Hit in D1 only :
$$P_{\text{independent}}(1\,\&\bar{3}) = P(1) \times P(\bar{3}) \quad (3c)$$
d. Hits in D1 &D3 :
$$P_{\text{independent}}(1\,\&3) = P(1) \times P(3). \quad (3d)$$

These cases were evaluated for particle tracks that–according to the silicon telescope–went through both detectors under study. Owing to a transverse misalignment, the geometrical overlap between the two detectors was rather small. The number of tracks that were available for this investigation was only 752 out of almost 5000 tracks recorded in total. Table II compares the measured probabilities for the four combinations of hits and misses with the calculated values assuming independence.

These results show a strong correlation between the measured failures in 1 and 3. In particular, simultaneous measured failures in 1 and 3 (row a) are far larger than predicted, while individual failures (rows b and c) are far less likely. This discrepancy is significant enough to show that the two detectors were not independent and that an extra systematic effect took place during data taking. The correlated efficiencies can be modeled by including a single common readout efficiency factor η. Each type of combined probability, under this assumption can be written as the product of the individual probabilities as in (3) above times η. In addition, the probability of detecting nothing (the top line in (4)) has a contribution of $(1-\eta)$ when (1) and (3) can be anything. The sum of the four probabilities is then $(1\times\eta)+(1-\eta)=1$. The four combined hit probabilities can then be written as

$$\begin{aligned} P(\bar{1}\,\&\bar{3}) &= P(\bar{1}) \times P(\bar{3}) \times \eta + (1-\eta) \\ P(\bar{1}\,\&3) &= P(\bar{1}) \times P(3) \times \eta \\ P(1\,\&\bar{3}) &= P(1) \times P(\bar{3}) \times \eta \\ P(1\,\&3) &= P(1) \times P(3) \times \eta. \end{aligned} \quad (4)$$

Solving this equation system yields the bare efficiencies as

$$P(1) = 94\%; P(3) = 97\%; \eta = 84\% \quad (5)$$

which are close to expectation. In addition, these numbers agree well with the estimates from the signal-to-noise distributions.

VII. EFFICIENCY AND SIGNAL WITHIN DETECTOR CELLS

A. Cell Mapping

A cell of the 3D detector away from the physical edges is defined in Fig. 6, with a p-electrode at the center and n-electrodes at each corner of the cell. The electrodes are expected to have lower detection efficiency. They are made of polycrystalline silicon with grain boundaries that allow many dangling bonds,

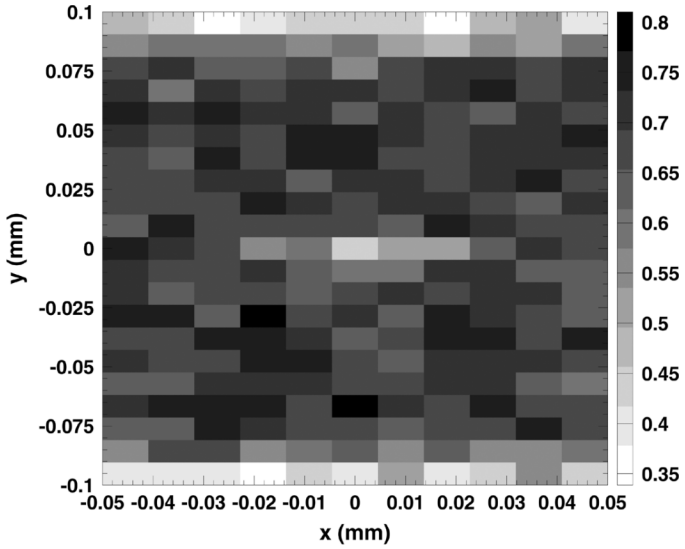

Fig. 15. The efficiency within a 3D detector cell is mapped according to the position of tracks predicted by the silicon telescope. It is plotted with an 11 by 21 grid, 86.6 μm^2 per square. The lower efficiency at the p-electrode in the center and under the aluminum line connecting n-electrodes is clear.

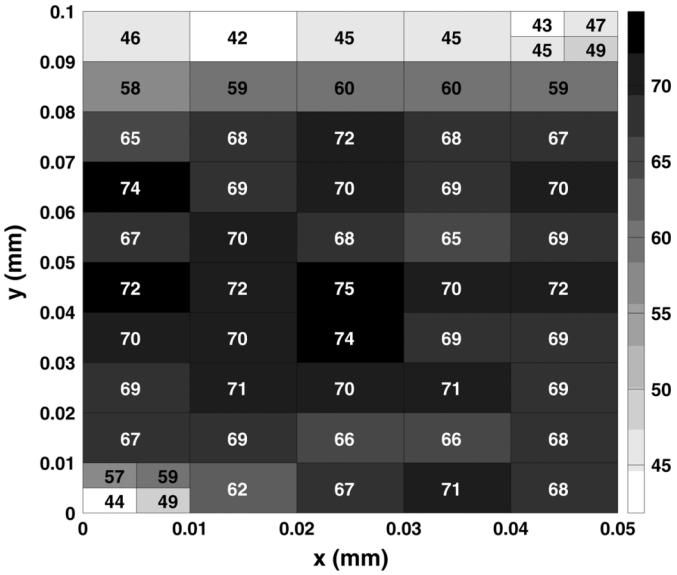

Fig. 16. Efficiency (%) projected on the upper right cell quadrants with p and n-electrodes in the lower left and upper right corners respectively. The segmentation is 10×10 μm^2 per square, except for the electrode corners which are subdivided in 5×5 μm^2 squares. The statistical error of the efficiency is 4 % for the small corner squares and 2 % for the others.

not all of which will be passivated with hydrogen from the silane used in the deposition. They are also highly doped, and would—if depleted—have high electric fields and injected currents, and so are not depleted under normal biasing conditions.

The efficiency with respect to position was measured using the predicted location of the particle tracks from the telescope by taking the number of hits recorded by 3D detectors and dividing by the predicted number. Tracks predicted to pass through the detector that counted gave an image of the detector shown in Fig. 12. This two-dimensional plot was not sufficient to show inefficient electrode regions due to low statistics. To increase the statistics, a three times larger data set was chosen (unfortunately with a slightly lower overall S/N ratio due to lower bias voltages). Furthermore, the data from detectors 1 and 3 were merged, and cells away from the edge of the detector were superimposed, giving a total of 44 880 events. Each 100 μm by 200 μm cell was subdivided into 11×21 rectangles, each about 9.09 μm $\times$ 9.52 μm, with the center one centered on a p signal electrode. This segmentation was chosen to be as fine as possible, but was limited by the spatial resolution of the telescope and by the need to have adequate statistics in the individual segments. The rms shift in track location across the 180 μm thick sensor due to the beam angular spread (0.7 mrad in x and 0.5 mrad in y) is 0.13 μm in x and 0.09 μm in y. This is negligible compared to the rectangle size of this study and also compared to the diameter of the electrodes.

No correction was made for the low system efficiency (84%) derived in Section VI.B, since we were just studying the relative efficiencies of the electrodes and the surrounding single crystal silicon. Fig. 15 shows the average efficiency over a cell.

Since the results for the four cell quarters were similar, a further mapping superimposed these results onto the upper right quadrant (shaded rectangle in Fig. 6), yielding Fig. 16. The upper right and lower left corner squares, which have n- and p-electrodes centered on their outside corners, are further

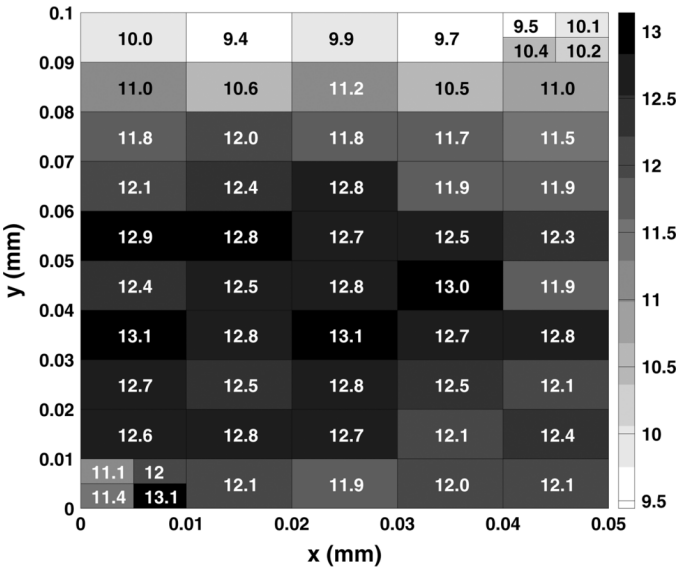

Fig. 17. The mean S/N ratio with a threshold of 5, mapped on the upper right quadrant of a cell. The statistical error is 0.4 for the small corner squares and 0.2 for the others.

subdivided into four squares of 5×5 μm^2 area. The p-electrode square and, to a lesser extent, the charge-sharing region between adjacent p-electrode channels have a lower efficiency compared to the average. The n-electrode square in the upper right corner of Fig. 16 does not differ significantly from the rest of the charge-sharing region under the n-n connecting aluminum strips.

A similar mapping study has been made for the signal-to-noise ratio. The S/N distribution is shown over a quarter cell in Fig. 17. As expected from the efficiency study, the regions under the n-n connecting strips also exhibit a lower S/N value

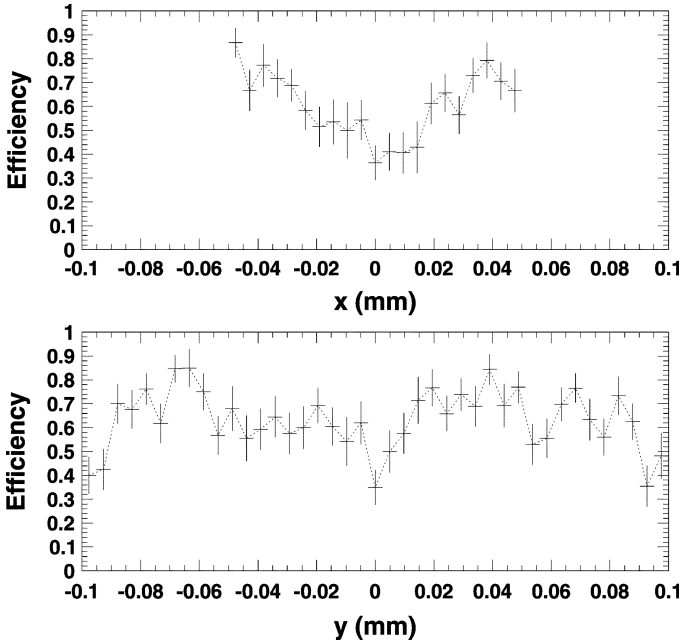

Fig. 18. Efficiency along 5 μm wide horizontal (top) and vertical (bottom) bands through the p-electrodes of the superimposed detector cells.

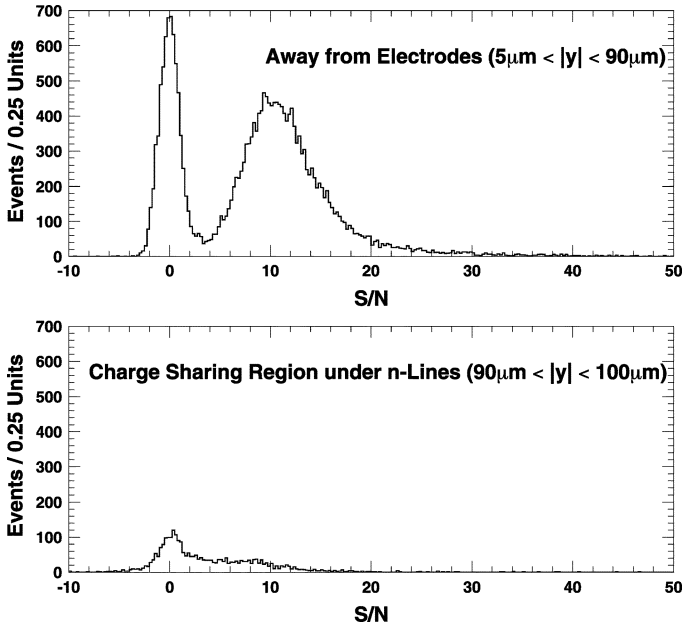

Fig. 19. S/N distributions in the bulk and in the charge-sharing region under the n-n connecting strips. The reference point ($y = 0$) is defined as the center of the p-electrode in a cell map.

than the remainder of the cell. The reduction at the p-electrode is also visible but less pronounced.

Both of these efficiency and pulse height reductions were expected. In the case of the electrodes, the electric fields are low and the charge carrier lifetimes short. The following sections focus on the different regions of reduced S/N and efficiency. To further understand the test-beam results, they are compared with X-ray measurements and simulations.

B. Electrode Efficiency

From the distribution of the full 100 μm by 200 μm cell in Fig. 15, the counts in 5 μm wide horizontal and vertical bands centered on the p-electrode are plotted with their corresponding statistical errors in Fig. 18. The measured efficiency for the p-electrodes is $(35 \pm 7)\%$ averaged over a 5 μm $\times$ 5 μm square centered on the electrodes, about 50 % of the plateau efficiency $(\approx 70\%)$ away from the p-electrodes and from the n-n connecting strips.

Similar 3D active edge detectors were also tested using X-rays at the Lawrence Berkeley Laboratory Advanced Light Source and with the GSECARS bending magnet beamline at the Advanced Photon Source at the Argonne National Laboratory [6]. The Advanced Light Source beam's full width at half maximum was 2.7 μm. Studies there show that within a radius of 3 μm from the p- and n-electrode centers the charge signals have a mean amplitude of 43 % and 62 % respectively, relative to the signal height in the bulk away from the electrodes. The FWHM of the regions with reduced signal amounts to 15 μm and 10 μm respectively.

The electrode studies with the muon beam thus show qualitative agreement with results from the Lawrence Berkeley Laboratory using X-rays. However there are significant differences in the methods of data collection, so quantitative comparisons cannot be made. In addition, there was a timing requirement and a separate pulse height threshold before a muon beam event was accepted for analysis. Both results show that the electrodes have some sensitivity, with n-electrodes more efficient than the p-electrodes. The physical differences responsible for this are yet to be identified, but there are several possibilities:

1. To develop a signal from radiation in a p (n) electrode, electrons (holes) must escape. They have different diffusion rates and lifetimes in polycrystalline silicon.
2. The dopant gases available at SNF produce an oxide layer on the etched hole surface which remains after the hole is filled and may produce oxide inclusions [20]. They will differ in radii and effectiveness as barriers.
3. The n-electrodes are made before the p-electrodes, and so are at high temperature for a longer time. During this time their grain size will increase, and this produces an increase in lifetime, increasing the charge collection efficiency [21], [22].

A full description of this efficiency data will also have to explain the lack of low pulse height tails, for example in the Gaussian spectral line shape of the 14 keV Neptunium L X-ray line shown in Fig. 7 of [9]. Any volume of partial, rather than total or zero, charge collection must be a small fraction of the total sensor volume.

Fabrication runs with variations affecting points 2 and 3, measurements with X-ray micro beams, and more detailed charge generation and collection simulations are planned to address these questions.

VIII. Signals in the Charge-Sharing Region and in Neighboring Channels

A. Observations

The signal reduction in the charge-sharing region, discovered in the cell maps in Figs. 15, 16, and 17, is further illustrated by the full S/N distributions in Fig. 19.

To understand this observation, the data were examined in several different ways. Fig. 20, showing the equipotentials, and

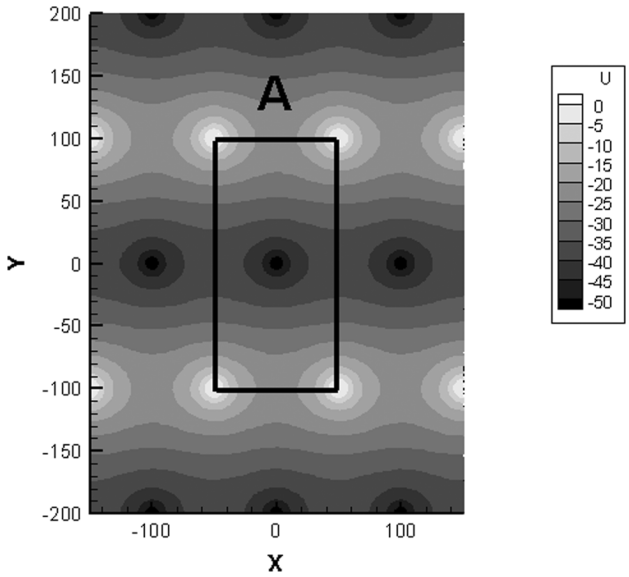

Fig. 20. Equipotentials at 3V intervals, for the 3D structure. The unit cell is indicated by the rectangle. p-electrodes are at $y = -200, 0$ and 200 μm. n-electrodes are at $y = -100$ and 100 μm. Charge sharing between strips occurs for particles traversing the detector near the line indicated by A due to the vanishing electric field component E_y. Charge spreading across the vertical boundaries remains in the same channel (see Fig. 6). The reverse bias is 50 V.

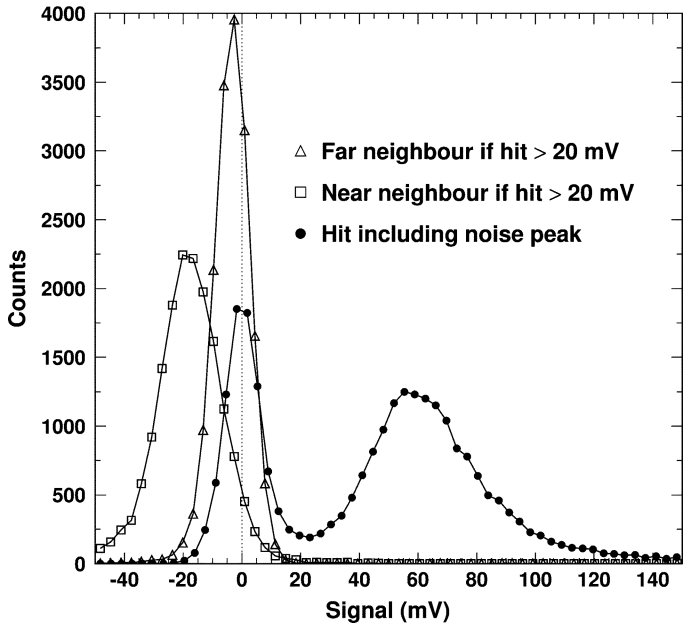

Fig. 22. Pulse height distributions from the test beam data on (solid circles) the hit electrode (that collects the ionization charge), and (squares) the near and (triangles) far neighbors for hit electrode signals > 20 mV at the preamplifier output.

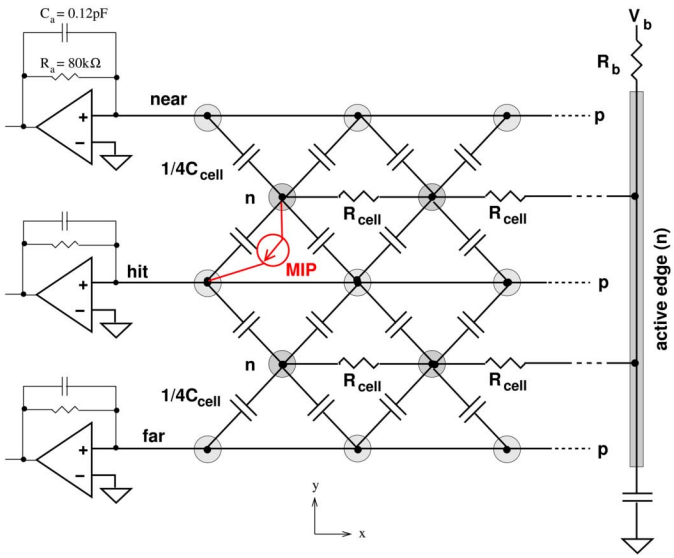

Fig. 21. Simplified circuit diagram of a 3D detector with front-end electronics. A track passes above the p-electrode array labeled as "hit" and induces a hit there. In this case, the upper neighboring p-electrode array is the near neighbor. For track positions below the hit electrode, "near" and "far" would be swapped. $R_{\rm cell}$–not part of the intended detector design–is the resistance of the charge sheets connecting the n-electrodes of an array, as explained later in the text. There were 38 electrodes for each horizontal line.

Fig. 21, a schematic diagram of the sensor and front-end electronics, are useful for this purpose.

The track in Fig. 21 ("MIP") traverses the upper half of the detector cell outlined in Fig. 20. Fig. 22 shows the pulse height distributions from the hit and two neighboring electrode channels for a track in this region. Here the "near" neighbor channel is the row of p-electrodes at the top of Fig. 21, the hit is in the middle, and the "far" is along the bottom.

The hit electrode channel has a noise peak centered on zero due to the same false or mis-timed triggers discussed in Section 6.2 and a peak with Landau broadening near 60 mV. The far electrode has a peak, consisting clearly mostly of noise, but sitting slightly on the negative side (-4.4% of the Landau peak). The near neighbor has a much more negative peak with an amplitude centered at 35 % of that of the hit channel, and is also wider. This unexpected observation of negative pulses is possible because the SCTA chip is able to record signals of both polarities.

The relation between the pulse height H in the hit channel and in the near neighbor is shown in the scatter plots of Fig. 23, distinguishing two cases based on the track position prediction from the beam telescope: (a) hits in the central region ($|y| < 90$ μm) of a detector cell, and (b) in the cell edge region ($90\,\mu{\rm m} < |y| < 100$ μm). The noise peak centered at (0, 0) from incorrect hits is clear, as is the Landau distribution of the hits H which is further widened by noise. However, even in the region far from the cell edge, where no charge sharing can take place, this distribution does not lie along the plot's abscissa as it would be expected, but rather at an angle whose tangent is about -0.31. Thus the near neighbor has a negative pulse with a magnitude of about 31% of the hit channel.

In the border region (Fig. 23(b)), besides

1. a similar noise peak and
2. a Landau distribution of somewhat smaller amplitude along a similar down-sloping line, there are
3. points directly above the Landau distribution for hit signals, and
4. points with positive amplitudes above noise levels for neighbor signals with near-zero and negative hit-values.

Group 3 points, a small fraction of the total, are from charge-sharing events.

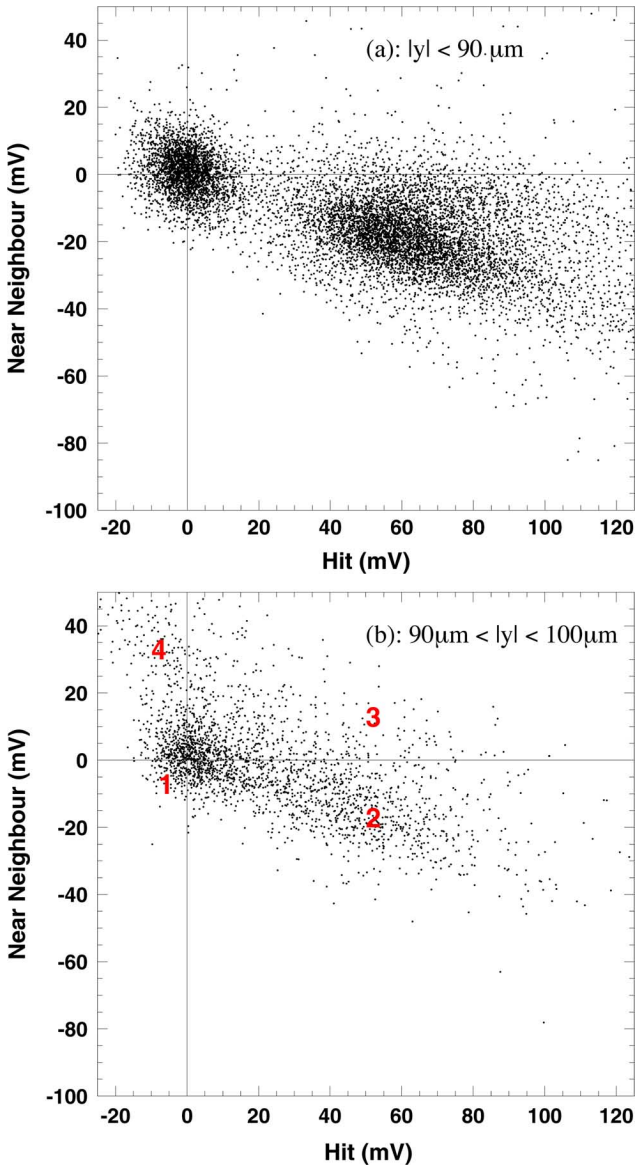

Fig. 23. Scatter plot of neighbor pulse height vs. hit channel pulse height for $|y| < 90\ \mu$m (a) and channel edge region $90 < |y| < 100\ \mu$m (b). The numerical labels in (b) are explained in the text.

Group 4 points are due to hits in the neighboring channel which were incorrectly predicted to be in the central channel. Given the known resolution of the beam telescope, this is quite reasonable. A negative signal $(H < 0)$ can be seen on the channel which was predicted to have the hit, but which in reality was the neighbor and hence did not have it.

Fig. 24 shows the interplay between the negative pulse phenomenon and charge sharing near the cell borders: the mean values of the pulses on the near and far neighbors are drawn as a function of the predicted y value of the track intersection. The behaviors in the upper and lower halves of the cell are symmetrical. The negative pulses are most prominent in the near neighbor when the track passed far from the cell border, whereas in the charge-sharing region near $y = \pm 0.1$ mm the negative pulse is partly compensated by positive charge arriving at the neighbor.

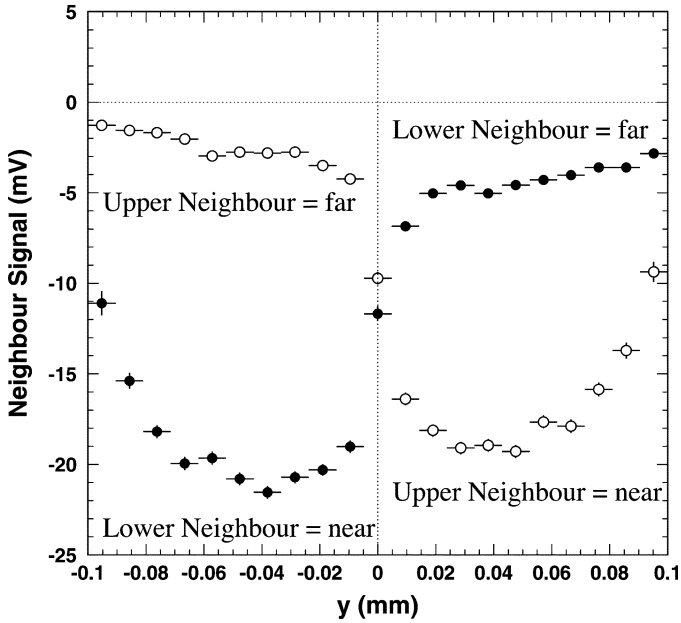

Fig. 24. Mean signal in the lower and upper neighbor as a function of calculated track position relative to the hit p-electrode. For $y < 0 (> 0)$, the lower (upper) neighbor is the near neighbor and exhibits the largest negative feed-through signal. The vertical error bars are given by rms noise divided by the square root of the number of hits for each point.

B. Cause of the Negative Signals in the Neighbors

The experimental observations can be explained by negative charge remaining on the n (bias) electrodes, inducing a negative signal on the neighbor and reducing the positive signal on the hit electrode. This charge would normally be collected rapidly by the lines to the power supply. To find the source of this delay, one of the sensors was examined in the laboratory. The aluminum bus lines were cut before the last electrode (between n1' and n2' in Fig. 4) on three of the bias lines to isolate them. The resistance was then measured between the aluminum line close to the electrode n1' (between n1' and c in Fig. 4) and the aluminum directly on the electrode n1'. It was found to be greater than $10^{10}\Omega$. This problem was caused by gaps between the metal bus line and the metal on the n-electrode tops. These electrode tops and also the metal on them had a lower surface level due to the etching step that removed the polycrystalline silicon deposited on the oxide during the hole-filling step. The aluminum used in this early fabrication was not thick enough to span this level shift.

This means that the return current was being carried on the relatively high-resistance charge sheets attracted to the silicon/oxide interface and narrowed along a route under the metal lines by the repulsive forces of the 3D anodes. The behavior of such a charge sheet was described in Figs. 9 of [2] and 18 and 19 of [3] and adjacent text.

The devices used here had no boron field implant (p-spray). The charge sheets consisted of mobile electrons, rather than trapped electrons around boron atoms. With such an implant, boron atoms (having one fewer valence electron than silicon) would have replaced silicon atoms at some of the lattice points, leaving a vacancy in one of the four bonds. Conduction electrons attracted to the always present positive fixed oxide charge near

the oxide-silicon interface would fall into these vacancies and be relatively tightly bound in the valence band. In planar technology, this procedure is used to prevent mobile charge sheets from shorting n-type electrodes.

Under bias there are large lateral forces repelling the (now mobile) charge from the p signal electrodes and attracting it to the n bias electrodes. At the 40 V operating bias, this charge sheet still joined the n-electrodes, but was well removed from the p-electrodes. The existence of gaps in the metal bias system tended to keep the charge sheet continuous. Any break in the sheet would have caused the now-isolated portion of the sheet to accumulate electrons from leakage and signal currents, and to grow in size, restoring continuity.

A charge sheet resistance calculation is given in the Appendix.

IX. Conclusion

For the first time silicon 3D detectors with "active edges" have been tested in a high energy particle beam. These tests demonstrate that this novel type of device can detect high-energy charged particles with an efficiency of 98 % to within 5 μm of its physical edge. The measured sensitive width is equal to the known physical width within less than 10 μm. These results, together with their radiation tolerance and signal speed characteristics, make 3D detectors strong candidates for forward proton tagging detectors at the LHC. Moreover, studies of the track response of the detectors show non-zero sensitivity in the 3D electrodes -50% and 67% of the plateau response for the p- and n-electrodes respectively, in qualitative agreement with previous results obtained with high resolution X-ray beams. Breaks in the bias electrode busses caused a reduction in signal height in the strips hit, along with negative signals in the neighboring strips, but did not change any of these conclusions. SPICE simulations of the equivalent device circuit confirmed the experimental observations. Additional details can be found in [23].

Note that deliberately slow charge collection from bias electrodes combined with a comparison of the two neighboring pulse heights (Fig. 24) could be used to improve the spatial precision because one can infer which side of the central electrode the particle has traversed [24].

Appendix
Approximate Calculation–Charge Sheet Resistance and Discharge Time-Constant

A. Charge Density

Charge is attracted by the fixed oxide charges normally present in silicon-silicon oxide interfaces. In single-crystal silicon and in the absence of field implants, this charge is mobile and affects both the sheet resistance and inter-electrode capacitances. To estimate these effects we must first determine the fixed oxide charge density.

The density per unit area of the fixed, positive charge at the interface has been measured to be

$$\rho_{\rm ox} = 2.6 \times 10^{11} e/{\rm cm}^2, \tag{6}$$

where e is the electron charge. This measurement was done by shining a pulsed infrared light beam on a region extending to the signal electrode wire-bond pad and centered about the "IR" in Fig. 4 (but actually located between the bottom two electrodes in Fig. 3—the edge signal wire-bond pad and below it, the bias electrode pad).

When the net surface charge density on the pad metal is negative and equal in magnitude to the fixed positive charge density in the oxide underneath, there is no net attractive or repulsive force for charges in the substrate. When the density becomes more positive (i.e., upon application of a positive bias voltage), electrons are attracted and form a conducting sheet under the metal that could contact n-type electrodes if there were a metal trace from the pad to n-electrodes. When on the other hand the charge density on the pad metal is made more negative (which was done for this test by applying a negative voltage), holes are attracted and can form a sheet that contacts p-type electrodes. The conductivity transition due to the hole sheet creation happens at the metal-to-substrate voltage difference of

$$V_{\rm tr} = -t\frac{\rho_{\rm ox}}{\varepsilon_{\rm ox}} \tag{7}$$

where t is the oxide thickness of 0.7 μm and $\varepsilon_{\rm ox} = 3.9\,\varepsilon_0 = 34.5 \times 10^{-12}$ As/Vm is the (absolute) dielectric constant of the silicon dioxide. The transition voltage $V_{\rm tr}$ was measured to be -8.5 V. For $V > -8.5$ V, i.e., without the nearby conducting channel to the electrode p2', the infra-red generated holes and electrons largely recombine, and no current signal is seen in the p-electrodes. For $V < -8.5$ V the hole sheet extends the electric field and the depleted silicon from the region around p2' to the region adjacent to the wire-bond pad. This region is illuminated by the infrared light, and sends the hole current to p2' which is drained to the biased pad via the aluminum line.

B. Charge Sheet Resistance

The electron density $\rho_{\rm sheet}$ in the charge sheet tends to the same density as the fixed oxide interface charge ($\rho_{\rm ox}$). A charge sheet of length s and width w containing that density of electrons has a resistance

$$R_{\rm sheet} = \frac{V}{I} = \frac{Es}{E\mu\rho_{\rm sheet}w} = \frac{s}{\mu\rho_{\rm sheet}w} \tag{8}$$

where E is the electric field, and μ is the mobility. Since the sheet is pulled up to the charged oxide, inducing scattering of charges moving along the interface, charges in it have a reduced mobility that depends on the perpendicular component of the electric field. The largest values of mobility (giving the lower limit for $R_{\rm sheet}$) in field effect transistors are about 800 cm^2/Vs, about half of the bulk mobility. Given the horizontal forces which narrow the sheet between the n-electrodes, the dimensions of the charge sheet in one 3D detector cell (Fig. 6) fulfill the relationship $s/w \geq 100\ \mu{\rm m}/200\ \mu{\rm m} = 0.5$. There are two charge sheets per cell, one per detector surface, each with a resistance of

$$R_{\rm sheet,cell} \geq 1/(2\,\mu\rho_{\rm sheet}) \approx 15\ {\rm k}\Omega, \tag{9}$$

leading to a total cell resistance $R_{cell} \geq 7.5\ {\rm k}\Omega$.

C. Electrode Capacitance

The capacitance $C_{\rm electrode}$ of a single, isolated 121 μm long electrode in a 100 μm $\times$ 200 μm pixel has been measured to be in a range between 0.04 pF [25] and 0.19 pF [10]. For the following discussion, only the order of magnitude is important, and a typical value of 0.1 pF will be used. Here, with 180 μm long n-electrodes, connected with other n-electrodes in the same column by the charge sheets,

$$C_{\rm cell} = (180/121) \times (2/3) \times 0.1\ {\rm pF} = 0.1\ {\rm pF}, \qquad (10)$$

where the factor of 2/3 comes from the fact that 2 of the 6 neighbors are n-electrodes tied to the one receiving the electrons.

The individual cell resistances $R_{\rm cell}$ and capacitances $C_{\rm cell}$ were combined with the preamplifier characteristics of ${\rm gain} = 1778$ and ${\rm RC} = 9.6$ ns (the subsequent shaping stages leading to a final shaping time of 20 ns were not modeled) to give the circuit response using a SPICE calculation based on the diagram in Fig. 20. The qualitative result, however, can be seen directly.

D. Charge Motion and Induced Signals

Holes travel to the closest p-electrode, inducing a current in it equal to the dot product of the velocity and the weighting field [26]–[28] and once collected, rapidly enter the connected amplifier shown at the left in Fig. 21. Electrons travel even more rapidly to the n-electrode, also making a current pulse in the p-electrode. This pulse is usually smaller even though the electrons are faster because of the smaller weighting field at the electron location reflecting the smaller solid angle of the p-electrode there. After arriving at the n-electrode, the electrons slowly spread in both directions along the charge sheet under the n-strip. During all this time, the negative charge stays at the same average distance from the neighboring strips of p-electrodes and hence induces a long flat negative signal there. Then finally the charge reaches the active edge connection (right sides of Figs. 3 and 21) and starts to drain off.

The total resistance of the charge sheet under a strip with 38 n-electrodes is of the order of $38 \times 7.5\ {\rm k}\Omega \approx 0.3\ {\rm M}\Omega$ and the total capacitance about $38 \times 0.1\ {\rm pF} = 3.8$ pF, leading to an RC time constant for discharging the entire n-line of the order of a μs, far longer than the preamplifier time constant of 9.6 ns. Thus the exact shape and exact impedance of the charge sheet which sets that time also is not critical.

E. SPICE Simulation and Induced Signals

This was verified in the SPICE simulation. A current source, shown in the figure as "MIP" simulates the effects of the induction signals from the several-ns duration motion of the electrons and holes to the n- and p-electrodes. The simulation results show the following:

1. As expected, for current-source signals injected at a position of 5 or more cells from the collection end, the total charge on the n-line spreads slowly along its length, remaining in nearly full strength for hundreds of ns, up to about 1 μs for a hit at the remote end.
2. At the amplifier output, a fast signal is observed whose shape is determined by the amplifier RC time constant of 9.6 ns, almost irrespective of the position of the injected pulse along the n-strip. In all cases, the amplifier input sees a signal far longer than its own time constant.
3. For the same reason, the big uncertainty of $R_{\rm sheet}$ has very little relevance: $R_{\rm sheet}$ can be reduced by about two orders of magnitude or arbitrarily increased without significantly changing the output signal. The amplifier input signal's time constant becomes comparable to the one of the amplifier only for R below 100 Ω per cell.
4. The much smaller signal induced across the larger distance to the "far" line and amplifier (percent level) was also observed in this simulation.

The negative charge induces the same negative pulse on both adjacent p-electrode rows: the near neighbor and the center hit. Thus one can infer from the near-neighbor pulse height distribution (Fig. 22) with its peak at -21 mV that the hit electrode peak has an original value of 81 mV which is then reduced by the same negative pulse to the observed value of about 60 mV.

F. Induced Signal Calculation

With this understanding, the hit-vs.-neighbor distributions in Fig. 23 can now be understood quantitatively. Let U be the total signal induced by a deposited charge and u the part of it picked up by the neighboring channel due to charge sharing. In the absence of the negative-pulse effect, the observed hit and neighbor signals H and N would lie on a line given by

$$(H, N) = (U - u, u). \qquad (11)$$

Then the negative signal reduces both the hit and the neighbor signals equally by an amount *fU* to

$$(H, N) = (U - u - fU, u - fU). \qquad (12)$$

From the observation

$$\left.\frac{N}{H}\right|_{u=0} = -0.31 \qquad (13)$$

in the region without charge-sharing we obtain $f \approx 0.25$, which allows us to determine U and u by inversion of (12). In particular, this gives access to the original value of S/N outside the charge-sharing region and without the negative-charge effect:

$$U|_{u=0} = \frac{H}{1-f} = 1.31H \qquad (14)$$

i.e., ${\rm S/N} = 1.31 \times 11 = 14.4$ as measured in the laboratory and as expected from theory.

Equation (12) also shows that in the charge-sharing region, the hit signal H is reduced twice: in addition to the constant negative charge $(-fU)$, a part of the signal (u) is lost to the neighbor. This explains the reduced efficiency near the cell boundaries.

REFERENCES

[1] G. Anelli *et al.*, The TOTEM Collaboration, "The TOTEM Experiment at the CERN Large Hadron Collider," JINST 3 S08007, 2008. TOTEM Tech. Design Rep., CERN-LHCC-2004-002, 2004.

[2] S. Parker, C. Kenney, and J. Segal, "3D-A proposed new architecture for solid state radiation detectors," *Nucl. Instrum. Methods Phys. Res. A*, vol. A395, pp. 328–343, 1997.

[3] C. Kenney, S. Parker, J. Segal, and C. Storment, "Silicon detectors with 3D electrode arrays fabrication and initial test results," *IEEE Trans. Nucl. Sci.*, vol. 46, no. 4, pp. 1224–1236, Aug. 1999.

[4] C. Kenney, S. Parker, and E. Walckiers, "Results from 3D silicon sensors with wall electrodes: Near cell-edge sensitivity measurements as a preview of active-edges sensors," *IEEE Trans. Nucl. Sci.*, vol. 48, no. 6, pp. 2405–2410, Dec. 2001.

[5] C. Da Via, "Radiation hard silicon detectors lead the way," *CERN Courier*, vol. 43, p. 223, 2003.

[6] J. Morse, C. J. Kenney, E. M. Westbrook, I. Naday, and S. I. Parker, "The spatial and energy response of a 3d architecture silicon detector measured with a synchrotron X-ray microbeam," *Nucl. Instrum. Methods Phys. Res. A*, vol. A524, pp. 236–244, 2004.

[7] C. Kenney, J. Segal, E. Westbrook, S. Parker, J. Hasi, C. Da Via, S. Watts, and J. Morse, "Active-edge planar radiation sensors," *Nucl. Instrum. Methods Phys. Res. A*, vol. A565, pp. 272–277, 2006.

[8] S. Parker, C. Kenney, D. Gnani, A. Thompson, E. Mandelli, G. Meddeler, J. Hasi, J. Morse, and E. Westbrook, "3DX: An X-ray pixel array detector with active edges," *IEEE Trans. Nucl. Sci.*, vol. 53, no. 3, pp. 1676–1688, Jun. 2006.

[9] C. Kenney, S. Parker, B. Krieger, B. Ludewigt, T. Dubbs, and H. Sadrozinski:, "Observation of beta and x-rays with 3D architecture silicon microstrip sensors," *IEEE Trans. Nucl. Sci.*, vol. 48, no. 2, pp. 189–193, Apr. 2001.

[10] S. Parker and C. Kenney, "Performance of 3D architecture silicon sensors after intense proton irradiation," *IEEE Trans. Nucl. Sci.*, vol. 48, no. 5, pp. 1629–1638, Oct. 2001.

[11] C. Da Via, G. Anelli, J. Hasi, P. Jarron, C. Kenney, A. Kok, S. Parker, E. Perozziello, and S. J. Watts, "Advances in silicon detectors for particle tracking in extreme radiation environments," *Nucl. Instrum. Methods Phys. Res. A*, vol. A509, pp. 86–91, 2003.

[12] T. Angelescu and A. Vasilescu, "Comparative radiation hardness results obtained from various neutron sources and the Niel problem," *Nucl. Instrum. Methods Phys. Res. A*, vol. A374, pp. 85–90, 1996, (earlier papers are quoted here).

[13] G. Lindstrom *et al.*, "Radiation hardness of silicon detectors—A challenge from high-energy physics," *Nucl. Instrum. Methods Phys. Res. A*, vol. A426, pp. 1–15, 1999.

[14] G. Lindstrom *et al.*, "Radiation hard silicon detectors—Developments by the RD48 (ROSE) collaboration," *Nucl. Instrum. Methods Phys. Res. A*, vol. A466, pp. 308–326, 2001.

[15] C. Da Via and S. Watts, "Can silicon detectors survive beyond 10^{15} n/cm^2," *Nucl. Instrum. Methods Phys. Res. A*, vol. A501, pp. 138–145, 2003.

[16] M. Deile *et al.*, "ODYSSEUS: A silicon telescope for test beam experiments," ATLAS Communication ATL-COM-MUON-99-015, available from ATLAS Secretariat or from M. Deile, CERN.

[17] Stanford Nanofabrication Facility, Center for Integrated Systems Building, Stanford, CA. Website: http://snf.stanford.edu.

[18] J. Kaplon, "Fast bipolar and CMOS rad-hard front end electronics for silicon strip detectors," CERN-Thesis-2004-041, Geneva, Switzerland, Mar. 2004.

[19] J. Kaplon *et al.*, "Progress in development of the analogue read-out chip for silicon strip detector modules for the LHC experiment," in *Proc. 7th Workshop Electronics for the LHC Experiments*, Stockholm, Sweden, Sep. 10–14, 2001, CERN/LHCC/2001-034, 22 Oct. 2001.

[20] J. Hwang and D. Schroder, "Recombination properties of oxygen-precipitated silicon," *J. Appl. Phys.*, vol. 59, p. 2476, 1986.

[21] A. Ghosh, C. Fishman, and T. Feng, "Theory of the electrical and photovoltaic properties of polycrystalline silicon," *J. Appl. Phys.*, vol. 51, pp. 446–554, Jan. 1980.

[22] T. I. Kamins*, Polycrystalline Silicon for Integrated Circuit Applications*, 2nd ed. Norwell, MA: Kluwer, 1998, p. 198.

[23] A. Kok, "Signal Formation and Active Edge Studies of 3D Silicon Detector Technology," Ph.D. dissertation, Brunel Univ., Uxbridge, U.K., 2005.

[24] S. Parker, C. Da Via, M. Deile, T.-E. Hansen, J. Hasi, C. Kenney, A. Kok, and S. Watts, "Dual readout: 3D direct/induced-signals pixel systems," *Nucl. Instrum. Methods Phys. Res. A*, vol. A594, p. 332, 2008.

[25] J. Metcalfe *et al.*, "Capacitance simulations and measurements of 3D pixel sensors under proton exposure," in *Proc. Nuclear Science Symp. and Medical Imaging Conf.*, Honolulu, HI, Oct. 2007.

[26] S. Ramo, "Currents induced by electron motion," in *Proc. IRE*, Sep. 1939, vol. 27, pp. 584–585.

[27] W. Shockley, "Currents to conductors induced by a moving point charge," *J. Appl. Phys.*, vol. 9, pp. 635–636, Oct. 1938.

[28] G. Cavalleri, E. Gatti, G. Fabri, and V. Svelto, "Extension of Ramo's theorem as applied to induced charge in semiconductor detectors," *Nucl. Instrum. Methods*, vol. 92, pp. 137–140, 1971.